Research Article | Open Access

Microstructures

Lyu *et al. Microstructures* **2026**, *6*, 20260126 **DOI:**10.20517/microstructures.2026.97

Growth redox conditions and interface effects govern polarization switching speed, retention and reliability in epitaxial $Hf_{0.5}Zr_{0.5}O_2$ thin films

Xueliang Lyu#, Faizan Ali#, Florencio Sánchez, Ignasi Fina

Keywords:
Ferroelectric hafnia, HfO_2, ZrO_2, pulsed laser deposition

Citation: Lyu, X.; Ali, F.; Sánchez, F.; Fina, I. Growth redox conditions and interface effects govern polarization switching speed, retention and reliability in epitaxial $Hf_{0.5}Zr_{0.5}O_2$ thin films. *Microstructures* **2026**, *6*, 20260126. https://dx.doi.org/10.20517/microstructures.2026.97

Received: 6 May 2026 **First Decision:** 25 Jun 2026 **Revised:** 19 Aug 2026 **Accepted:** 27 Aug 2026 **Published:** 23 Sep 2026

Academic Editor: Dawei Wang **Copy Editor:** Fangling Lan **Production Editor:** Fangling Lan

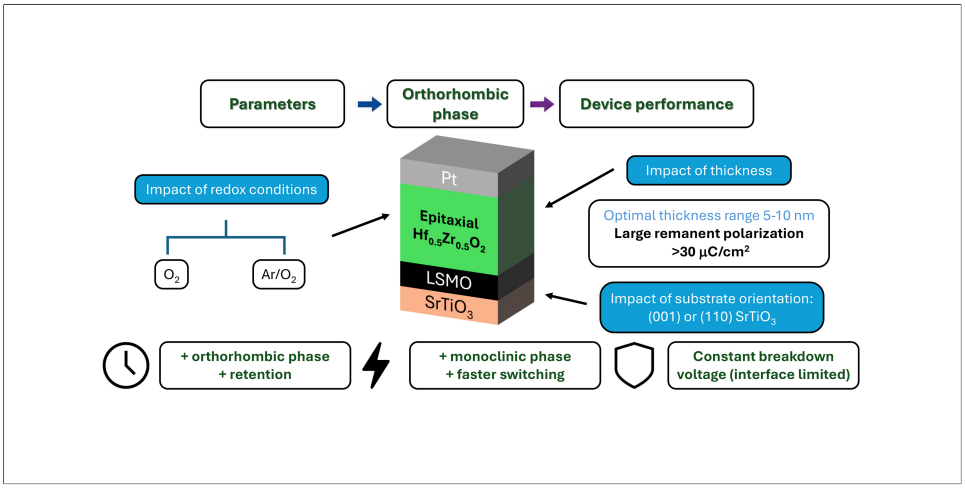

Abstract

Ferroelectric HfO_2-based thin films are promising for next-generation non-volatile memories. Achieving further understanding of how the interfaces and defects influence switching dynamics and reliability is essential for device optimization. Here, we investigate the polarization switching kinetics, breakdown strength, and retention of a series of epitaxial $Hf_{0.5}Zr_{0.5}O_2$ (HZO) of increasing thickness and grown using different oxidation conditions on substrates with different orientations. Time-dependent ferroelectric characterization shows that films in the intermediate thickness range (≈5-10 nm), which exhibit the largest remanent polarization (above 30 μC/cm^2), show slower switching. In addition, polarity-dependent switching kinetics is observed in ultrathin films, which is attributed to built-in electric fields associated with asymmetry between interfaces. Reliability analysis shows that the breakdown electric field decreases with increasing thickness, reaching up to ~55 MV/cm, while the retention remains stable in the optimal thickness range. These results demonstrate that the interplay between film thickness, interface symmetry, and oxidation conditions during growth governs the switching dynamics and reliability of epitaxial HZO films, providing guidelines for the design of high-performance ferroelectric devices.

Institut de Ciència de Materials de Barcelona (ICMAB-CSIC), Carrer dels Til.lers, Cerdanyola del Vallès 08193 Spain.
#Authors contributed equally.

Correspondence to: Dr. Florencio Sánchez, Dr. Ignasi Fina, Institut de Ciència de Materials de Barcelona (ICMAB-CSIC), Campus UAB, Barcelona 08193, Spain. E-mail: fsanchez@icmab.es; ifina@icmab.es

INTRODUCTION

Since the first report of ferroelectric response in HfO_2[1], this material has emerged as a key material for next-generation non-volatile memories[2,3], in particular in compositions such as $Hf_{0.5}Zr_{0.5}O_2$ (HZO)[4]. Several critical factors have been identified as influencing functional properties, and these include dopants, film thickness, interfaces, stress, and defects, particularly oxygen vacancies[5-12].

It has been demonstrated that epitaxial growth on perovskite substrates enables stabilization of the orthorhombic phase with high ferroelectric polarization[13,14]. The lattice mismatch is very large; however, the orthorhombic phase is epitaxially stabilized through the domain-matching epitaxy (DME) mechanism[15]. Contrary to conventional epitaxy, DME involves the formation of structurally relaxed grains during film nucleation. Epitaxial growth is enabled by the periodic insertion or absence of an extra crystal plane, which reduces the residual elastic strain. Consequently, DME strongly depends on the substrate or bottom electrode layer, as well as on the interface. Thus, interfaces play a decisive role in epitaxial HfO_2 films, and bottom electrode and/or substrate crystallographic orientation and symmetry mismatch have been shown to strongly impact ferroelectric orthorhombic phase formation[16-18]. In the widely investigated case of $SrTiO_3$ (STO) as a substrate and $La_{0.67}Sr_{0.33}MnO_3$ (LSMO) as the bottom electrode, the orthorhombic phase of HfO_2 crystallizes with (111) orientation (3-fold symmetry) on both STO(001) (4-fold symmetry) and STO(110) (2-fold symmetry) substrates[19,20]. Films on STO(110) have a higher orthorhombic phase content and lower monoclinic phase content than equivalent films on STO(001), indicating that residual stress in the film due to the interface mismatch is lower when using this substrate[20]. Consequently, higher ferroelectric polarization has been reported in doped HfO_2 films grown on (110)-oriented substrates[19-22]. However, the influence of substrate orientation on switching dynamics, retention, and breakdown electric field (E_{BD}) has not yet been systematically investigated.

Redox conditions during growth are also critical. Oxygen vacancies are known to influence the relative stability of competing polymorphs and can promote the formation of the ferroelectric orthorhombic phase when present in optimal concentrations[9,20,23-25]. While excessive oxygen deficiency may lead to leakage and reliability degradation, moderate reducing conditions have been shown to enhance polarization without compromising endurance in epitaxial HfO_2 films. On the other hand, cooling conditions after deposition of epitaxial films have little effect on functional properties[26]. In ferroelectric hafnia, fast polarization switching dynamics and long-term retention properties are also required, and in previous studies these have been linked to domain nucleation, domain wall motion, and defect-domain interactions, all of which are in turn also influenced by grain boundaries and oxygen vacancy concentrations[27-30]. Additionally, the coexistence of ionic dynamics with the ferroelectric phase can enhance the resistive ON/OFF ratio, increasing the functionality of the material and demonstrating its potential for integration into in-memory computing platforms[31].

Despite the extensive literature on phase stabilization and polarization enhancement in hafnia films, the impact of interface symmetry and redox growth conditions on switching kinetics and retention remains insufficiently explored in epitaxial systems. In this work, we address these questions by investigating the polarization switching behavior and retention properties of epitaxial HZO films on STO(110) and STO(001) substrates grown under different oxidation conditions. We show that switching kinetics and reliability are strongly governed by the interplay between film thickness, interface symmetry, and growth atmosphere.

EXPERIMENTAL

Two series of HZO films with thicknesses ranging from 4.5 to 18.1 nm were grown on STO(001) and STO(110) substrates buffered with a ~25 nm LSMO bottom electrode under an O_2 atmosphere with an oxygen pressure of 0.1 mbar (denoted as STO(001) O_2 and STO(110) O_2 series, respectively). Another series

of films with thicknesses ranging from 3.6 to 14.4 nm on STO(110) was deposited under an O_2/Ar atmosphere with an argon partial pressure of 0.05 mbar and an oxygen partial pressure of 0.05 mbar (denoted as STO(110) O_2/Ar series). Both the LSMO electrode and HZO layers were deposited sequentially in a single PLD process using a KrF excimer laser. The LSMO electrodes were deposited at a substrate temperature of 700 °C under an oxygen pressure of 0.1 mbar. The HZO films were deposited at 800 °C . After deposition, the samples were cooled immediately under 0.2 mbar of oxygen. Circular Pt top electrodes (20 μm diameter and 20 nm thickness) were deposited by DC magnetron sputtering through stencil masks for electrical measurements. Structural characterization was carried out by X-ray diffraction (XRD) using Cu Kα radiation in a Bruker D8 diffractometer equipped with a two-dimensional (2D) detector. Ferroelectric characterization was performed using a TFAnalyzer3000 platform (AixACCT GmbH), with the LSMO bottom electrode grounded and the bias applied to the Pt electrodes in a bottom-top configuration. For switching spectroscopy experiments, a pre-switching pulse was applied, which was long enough to ensure polarization saturation. Afterward, a trapezoidal switching pulse with a plateau and rise/fall time of t_w was applied. After 1 s, a pulse of opposite polarity to the writing pulse was used for polarization reading. The switched polarization (ΔP) was calculated from the subtraction of the values measured during X and U (i.e., X-U) or X and D (X-D), where X corresponds to the reading pulse. All polarization loops were recorded at 1 kHz. To compensate for leakage in polarization loops, the dynamic leakage current compensation was employed[32]. To determine the breakdown electric field, current-voltage characteristics were recorded using a voltage sweep from 0 to -30 V, then to +30 V, and finally back to 0 V over a total duration of 1 s.

RESULTS AND DISCUSSION

Figure 1A shows the XRD χ-2θ maps collected around the orthorhombic o-(111) reflection for all samples in the three series. The thickness of each HZO film is indicated above the corresponding diffraction map. In all cases, a sharp and well-defined diffraction spot corresponding to the o-(111) reflection is observed at 2θ ≈ 30°, indicating the stabilization of the orthorhombic phase. The nearly circular shape of the reflection confirms the high crystalline quality of the films and the absence of significant mosaic spread, consistent with epitaxial growth. For samples grown on STO(110), an additional, more intense reflection at 2θ ≈ 32.4°, originating from the substrate and the LSMO electrode, is also observed. As the film thickness increases beyond ~10 nm, an additional spot corresponding to the monoclinic m-(-111) reflection becomes visible for all the films. Compared to the orthorhombic reflection, this peak appears more elongated along the χ angle, indicating a larger mosaicity of the monoclinic crystallites.

To quantify the phase evolution, 2θ diffractograms were obtained by integrating the χ-2θ maps along χ within a range of ±10°, as shown in Supplementary Figure 1. From these integrated profiles, the area ratio between the monoclinic m-(-111) and orthorhombic o-(111) peaks was extracted and plotted as a function of film thickness in Figure 1B. The results reveal that for thinner films, only the orthorhombic phase is detected. As the film thickness increases, the monoclinic phase fraction also increases across all sample series. Similar epitaxial doped HfO_2 films exhibit a columnar grain microstructure, irrespective of whether the grains are orthorhombic or monoclinic, as consistently demonstrated by transmission electron microscopy in previous works[15,21]. The found thickness dependence trend is particularly pronounced for films in the STO(110) O_2 series. The structural evolution with thickness described above is schematically represented in the sketch of Figure 1C.

Figure 2A-C presents the positive-up-negative-down (PUND) polarization-electric field (P-E) hysteresis loops measured in the pristine state for the three series of samples. The corresponding current-electric field characteristics are provided in Supplementary Figure 2. All samples exhibit well-defined ferroelectric hysteresis loops, confirming the presence of switchable ferroelectric polarization. The thickness dependence of the remanent polarization (P_r) is shown in Figure 2D. The data reveal a non-monotonic behavior, with

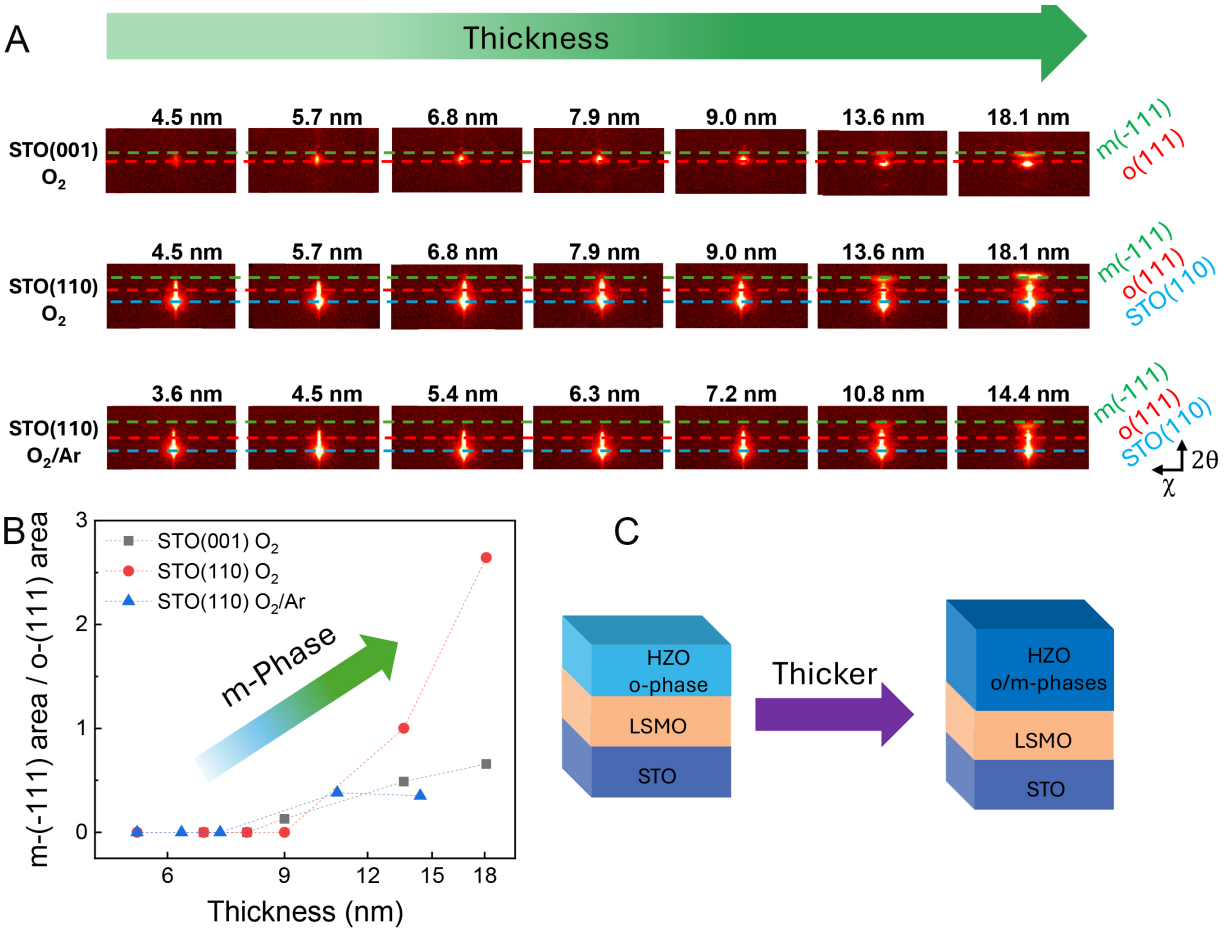

Figure 1. (A) χ-2θ diffraction images around the o-(111) reflection for HZO films of the indicated thickness for the three series: STO(001) O_2, STO(110) O_2, and STO(110) O_2/Ar. The orthorhombic (o) and monoclinic (m) reflections are indicated. (B) Area ratio of the m-(-111) diffraction peak with respect to the o-(111) peak, extracted from the χ-integrated 2θ patterns, as a function of film thickness for the three series of samples. (C) Schematic illustration of the thickness-dependent phase evolution of epitaxial HZO films, showing the stabilization of the orthorhombic phase in the ultrathin regime and the progressive appearance of the monoclinic phase with increasing thickness.

reduced P_r observed in both very thin and thick films. The P_r increases from ~8.6 μC/cm² for the 4.5 nm film to a maximum of 23.4 μC/cm² for the 9 nm film of the STO(001) O_2 series, whereas in the STO(110) O_2/Ar series, it reaches a maximum of 34.7 μC/cm² at 7.2 nm. The reduction of P_r in thinner films can be ascribed to dead-layer effects. The comparison of the STO(001) O_2 and STO(110) O_2 series shows that the polarization is consistently higher for films grown on STO(110) across the entire optimal thickness range. This observation is in agreement with previous reports, while extending them by demonstrating that the enhancement is systematic over a broad range of film thicknesses, rather than being limited to the comparison of single thicknesses[19,20,33]. Although Pt was selected as the top electrode due to its non-highly reactive nature, and LSMO was used because of its epitaxial compatibility with HZO, the presence of interfacial capacitance cannot be completely avoided. Such effects may occur either at the top Pt/ferroelectric-layer interface, probably due to defect accumulation[33] or at the bottom ferroelectric-layer/LSMO interface due to cation intermixing[34,35]. For thicker films, the remanent polarization decreases again, which is consistent with the increasing fraction of the non-ferroelectric monoclinic phase [Figure 1]. The coercive field dependence on thickness is shown in Figure 2E. A general decrease in the coercive field is observed as film thickness increases.

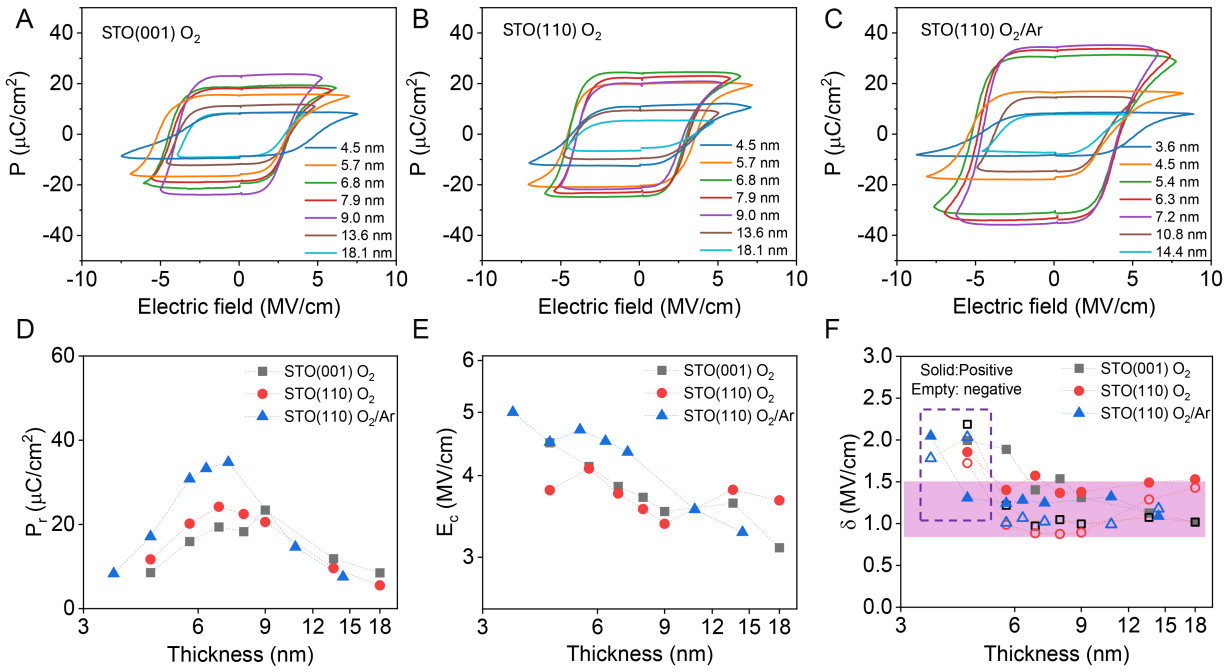

Figure 2. (A-C) Polarization-electric field (P-E) hysteresis loops measured using the PUND method for the three series of samples: (A) STO(001) O_2, (B) STO(110) O_2, and (C) STO(110) O_2/Ar. (D) Thickness dependence of the remanent polarization (P_r) for the three series of samples. (E) Thickness dependence of the coercive field (E_c). (F) Thickness dependence of the coercive field distribution parameter δ extracted from the fitting of the hysteresis loops.

To gain further insight into the switching characteristics, the P-E loops were fitted using a model describing the ferroelectric polarization response[36]:

$$P_{FE} = P_0 * \tanh\left(\frac{E-Ec}{\delta}\right) \quad (1)$$

where P_0 is the saturation polarization, E_c is the coercive field, E is the applied electric field, and δ represents the width of the coercive field distribution. This semi-empirical method provides a convenient measure of switching inhomogeneity represented by δ. The corresponding fits are shown in Supplementary Figure 3. The extracted values of δ are plotted as a function of film thickness in Figure 2F. The thinnest films exhibit the largest distribution, δ values reaching approximately 1.5-2.2 MV/cm, indicating a broader spread of local switching fields (enclosed by the dashed rectangle). The δ decreases with increasing thickness and then remains relatively small (~1.0-1.5 MV/cm), indicating that the switching process is more uniform.

Figure 3A-C shows the polarization time-dependent switching spectra measured using the PUND method (see Section "EXPERIMENTAL" for details) for the three series, under both positive and negative writing voltages (V_w). The leakage correction procedure is detailed in Supplementary Figure 4. The corresponding polarization-electric field loops obtained for different writing pulse widths are presented in Supplementary Figure 5. Most samples exhibit clear ferroelectric switching behavior, characterized by a rapid increase in ΔP with increasing t_w, followed by saturation at t_w > ~1 μs. STO(001) O_2 series shows relatively smaller switching amplitudes and a nearly symmetric response between positive and negative polarities, as shown in Figure 3A. In contrast, the STO(110) O_2 series exhibits a noticeably larger switching amplitude and a clear asymmetry between the two poling directions [Figure 3B]. An even stronger enhancement of ΔP, together with a more pronounced polarity dependence, is observed for the STO(110) O_2/Ar series shown in Figure 3C.

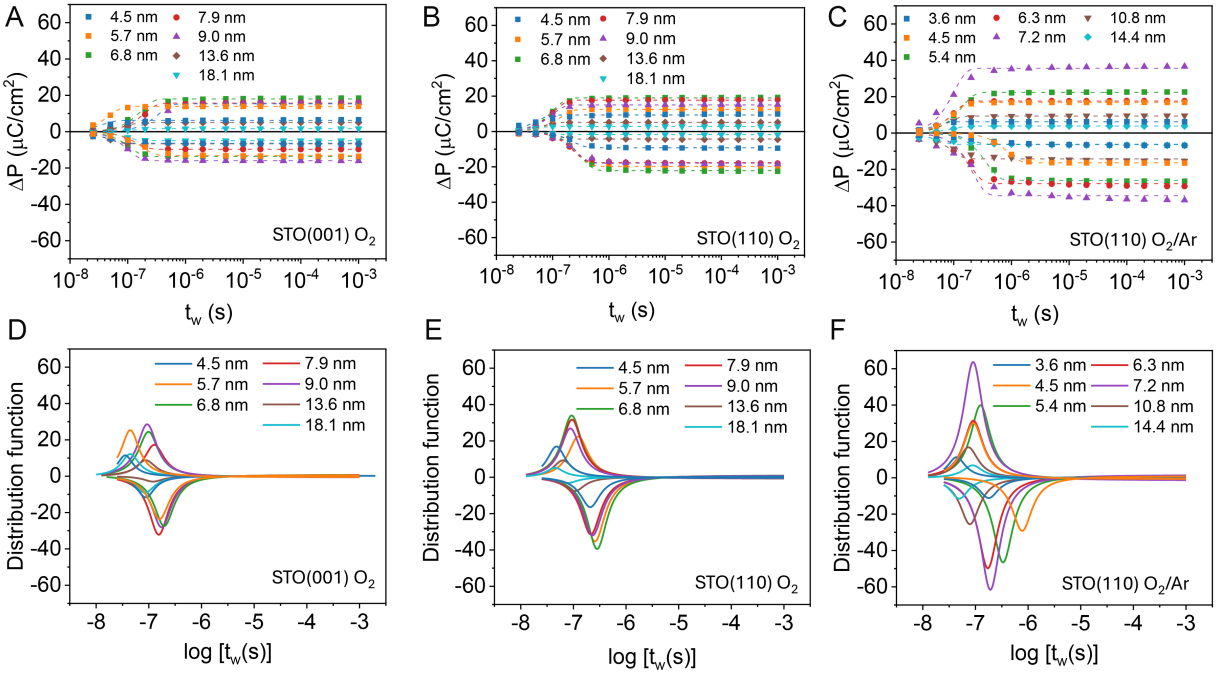

Figure 3. (A-C) ΔP as a function of writing pulse width (t_w) measured by PUND for the three sample series: (A) STO(001) O_2, (B) STO(110) O_2, and (C) STO(110) O_2/Ar. Dashed lines correspond to fits using the nucleation-limited switching (NLS) model. (D-F) Corresponding Lorentzian distributions of local switching times extracted from the NLS fitting for the three series of samples.

For the thinnest films (below ~5 nm), small variations in the shape of the I-V and P-V loops during the first cycles are observed [Supplementary Figure 6], although these variations remain relatively minor. In the case of the 4.5 nm STO(110) O_2/Ar series, where this variation is most noticeable, and a significant reduction in the switching time is observed after electrical cycling [Supplementary Figure 7]. This switching time reduction indicates that the redistribution of defects at the interface can influence the switching dynamics. To further analyze the switching kinetics, the experimental ΔP-t_w data were fitted over the entire experimental range using the nucleation-limited switching (NLS) model[37], which accounts for a distribution of local switching times:

$$\Delta P = 2P_r \int_{-\infty}^{+\infty} \left[1 - e^{-\left(\frac{t}{\tau}\right)^n}\right] F(\log \tau) \times d(\log \tau) \quad (2)$$

where n is the effective dimensionality of domain growth (fixed at $n = 2$), τ is the characteristic switching time, and F(logτ) is the Lorentzian distribution for the logarithm of switching time. The Lorentzian distribution can be expressed as:

$$F(\log \tau) = \frac{A}{\pi}\left[\frac{w}{(\log \tau - \log t_1)^2 + w^2}\right] \quad (3)$$

where A is a normalization constant, w accounts for the width of the distribution, and $\log t_1$ represents the central value of the distribution.

The extracted distribution functions are shown in Figure 3D-F, while the corresponding fitting parameters are summarized in Supplementary Tables 1-3. For STO(001) O_2 series, the switching time distribution is relatively narrow and symmetric for the two polarities, indicating similar switching dynamics under positive

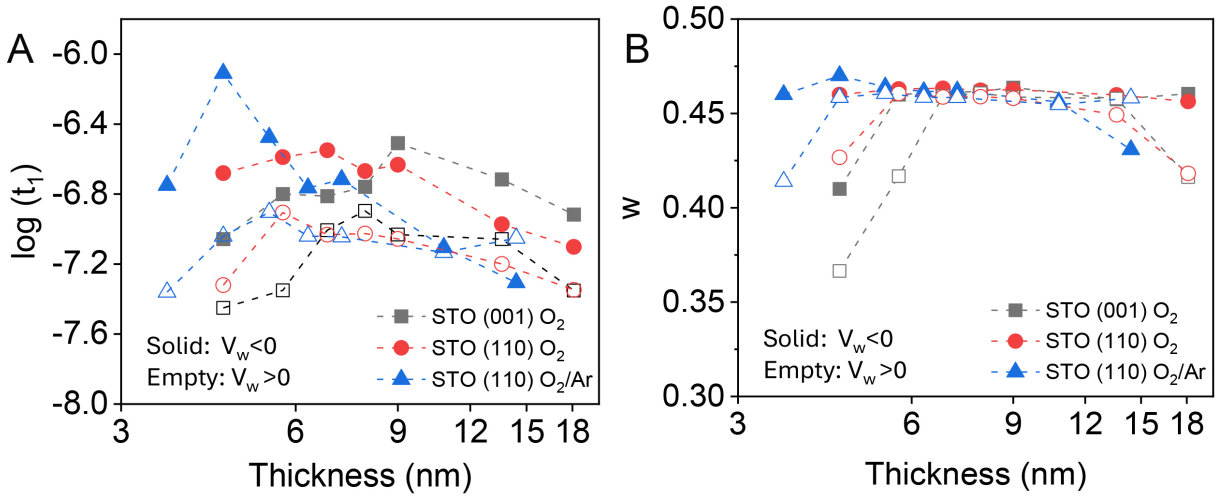

Figure 4. Thickness dependence of the switching parameters extracted from the NLS model fitting. (A) Characteristic switching time ($\log(t_1)$) as a function of film thickness and (B) width of distribution (w) of the switching time for the three series.

and negative fields. In contrast, STO(110) O_2 series exhibits broader distributions and a more pronounced and systematic difference between positive and negative switching times. This asymmetry becomes even more important for the STO(110) O_2/Ar series, where the switching distributions indicate faster switching for one polarity.

Figure 4A shows the thickness dependence of the characteristic switching time extracted from the NLS fitting of the switching spectroscopy data presented in Figure 3. The values are plotted for both positive and negative voltage polarities for the three sets of samples. For ultrathin films (thickness below ~6 nm), the characteristic switching time exhibits a pronounced dependence on the polarity of the applied electric field. In STO(110) O_2 series, the extracted values change from $\log(t_1)$ = -7.32 for positive polarity and -6.68 for negative polarity for the 4.5 nm film. A similar asymmetry is also observed for the STO(110) O_2/Ar series, where the 3.6 nm film shows -7.36 for positive polarity and $\log(t_1) \approx$ -6.75 for negative polarity.

As the film thickness increases, above ~9 nm, the characteristic switching time gradually shifts toward smaller values, and the difference between the two polarities becomes significantly reduced. In the STO(110) O_2 series, the switching time changes from $\log(t_1) \approx$ -6.6 in the 5-9 nm range to approximately -7.2 for films with thicknesses of 13.6-18.1 nm for the negative polarity ($V_w < 0$). The difference between positive and negative switching times decreases from $\log(t_1) \approx 0.60$ at 4.5 nm to less than ~0.15 for films thicker than ~13 nm. A similar trend is observed for the STO(001) O_2 and STO(110) O_2/Ar series. The observed reduction in switching time asymmetry for thicker films indicates that this is governed by the presence of defects at the interfaces, as discussed above[33-35] and further supported by the reduction in the imprint electric field with thickness [Supplementary Figure 8]. Figure 4B shows the thickness dependence of the w parameter obtained from the NLS fitting. The w values remain within a relatively narrow range of ~0.37-0.47 for all samples. Slightly lower values for the thinnest and thickest films are mainly attributed to the lower polarization of these films.

Figures 5A-C show the Weibull statistical distribution of the E_{BD} for the three sets of samples. Representative current-electric field curves used to determine the breakdown field for the different film thicknesses are shown in Supplementary Figure 9, except for the 3.6 nm film, which showed larger conductivity. The E_{BD} was defined as the electric field at which a sudden increase in leakage current indicates dielectric failure. This, in the present case, occurs for negative polarity. The Weibull relationship is expressed as[38,39]:

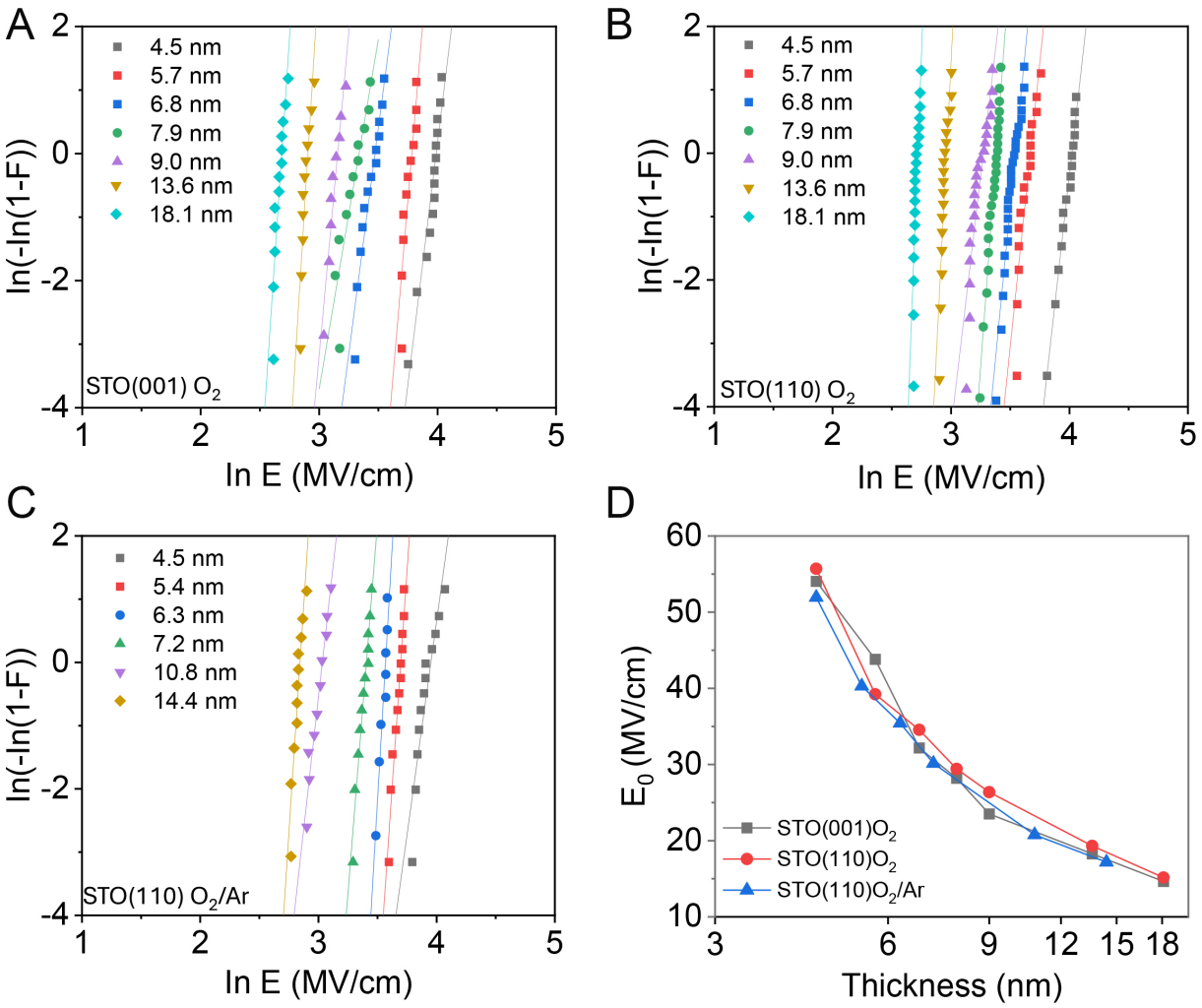

Figure 5. Weibull statistical distributions of the E_{BD} for the three series: (A) STO(001) O_2, (B) STO(110) O_2, and (C) STO(110) O_2/Ar. (D) Thickness dependence of the E_0 extracted from the Weibull fitting for the three series of samples.

$$\ln[-\ln(1-F(i))] = \beta \ln E - \beta \ln E_0 \quad (4)$$

where F(i) represents the cumulative breakdown probability, E is the applied electric field, E_0 is the characteristic breakdown electric field, and β is the Weibull slope describing the dispersion of breakdown events. As shown in Figures 5A-C, the plots of ln[-ln(1 - F(i))] *vs.* ln(E) exhibit linear behavior for all samples. The characteristic breakdown fields extracted from the Weibull analysis are summarized in Figure 5D as a function of film thickness. β values lie between ~15 and ~31 for all samples. A clear monotonic decrease in E_0 with increasing thickness is observed for all three series. The characteristic E decreases from ~55 MV/cm for the 4.5 nm film to about 15 MV/cm for the 18.1 nm films. In brief, the overall thickness dependence remains very similar across the three series, indicating that the dielectric breakdown strength is primarily governed by the film thickness. More careful data inspection allows us to infer that E_{BD} is slightly lower in O_2/Ar-grown films (see Supplementary Figure 10), suggesting a higher concentration of defects, most likely oxygen vacancies. These defects promote dielectric breakdown at lower electric fields, indicating that defect density acts as a secondary factor governing the breakdown strength.

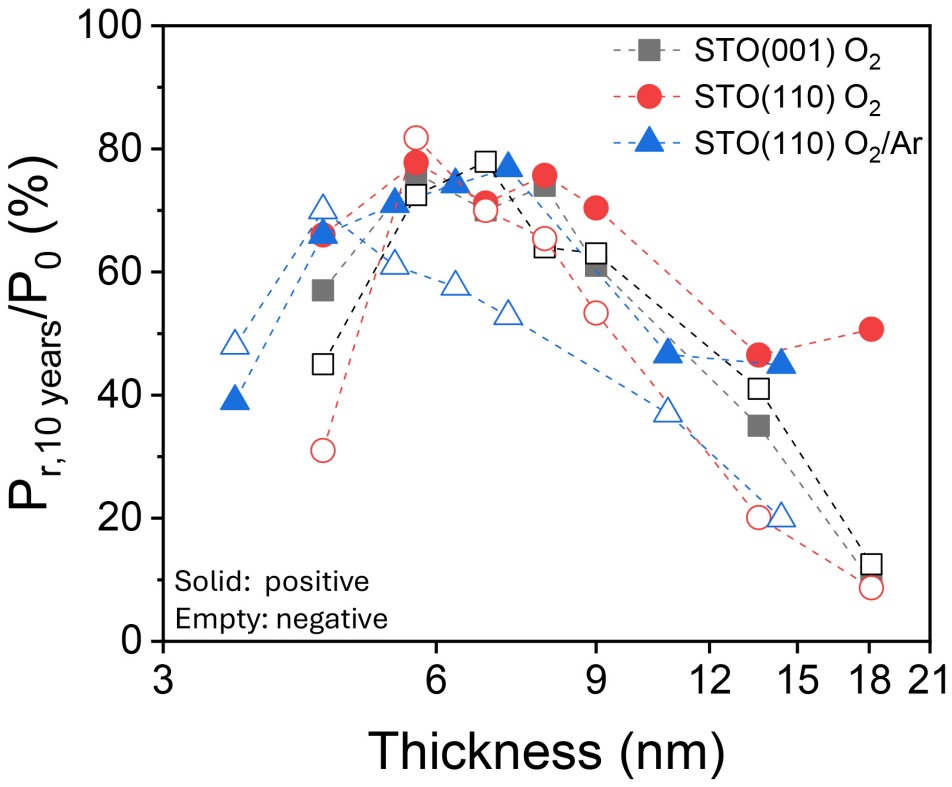

Figure 6. Retention performance of the three series, expressed as the remanent polarization extrapolated to 10 years and normalized to the initial value as a function of film thickness. Filled and open symbols correspond to the positive and negative polarization states, respectively.

Figure 6 summarizes the retention performance of the three series, evaluated from the remanent polarization extrapolated to 10 years and normalized to the initial polarization value, as a function of film thickness. The corresponding PUND loops and raw retention measurements used for the extrapolation are provided in Supplementary Figure 11. For films with thickness in the 5-10 nm range, both STO(001) O_2 and STO(110) O_2 series exhibit relatively stable retention, with more than 50% of the initial polarization preserved. In contrast, STO(110) O_2/Ar series shows a more pronounced asymmetry between the positive and negative polarization states. In particular, the retained polarization decreases to approximately 50%-60% for the negative polarization state, while the positive state remains comparable to the other series (≈70%-77%).

Figure 7 summarizes the relationship between the remanent polarization and switching time, dielectric breakdown strength, and retention. The numbers next to the data points indicate the corresponding film thickness in nm, allowing the role of thickness to be directly visualized in the correlations. Figure 7A shows the dependence of the characteristic switching time on the remanent polarization for positive polarity. A general correlation between polarization magnitude and switching time is observed. Films with low polarization tend to exhibit relatively faster switching dynamics. Note that the obtained low switching times are very close to the time constant of the experimental setup, measured in detail in ref.[40], thus influenced by that.

Figure 7B shows the absence of direct correlation between remanent polarization and the dielectric breakdown field. E_{BD} increases with polarization for low E_{BD} values, while it decreases for high E_{BD} values. This non-monotonic behavior reflects the thickness dependence of polarization, which first increases and then decreases with increasing film thickness. Therefore, it can be concluded that E_{BD} is mainly determined by film thickness. The correlation between polarization and retention stability is shown in Figure 7C. The

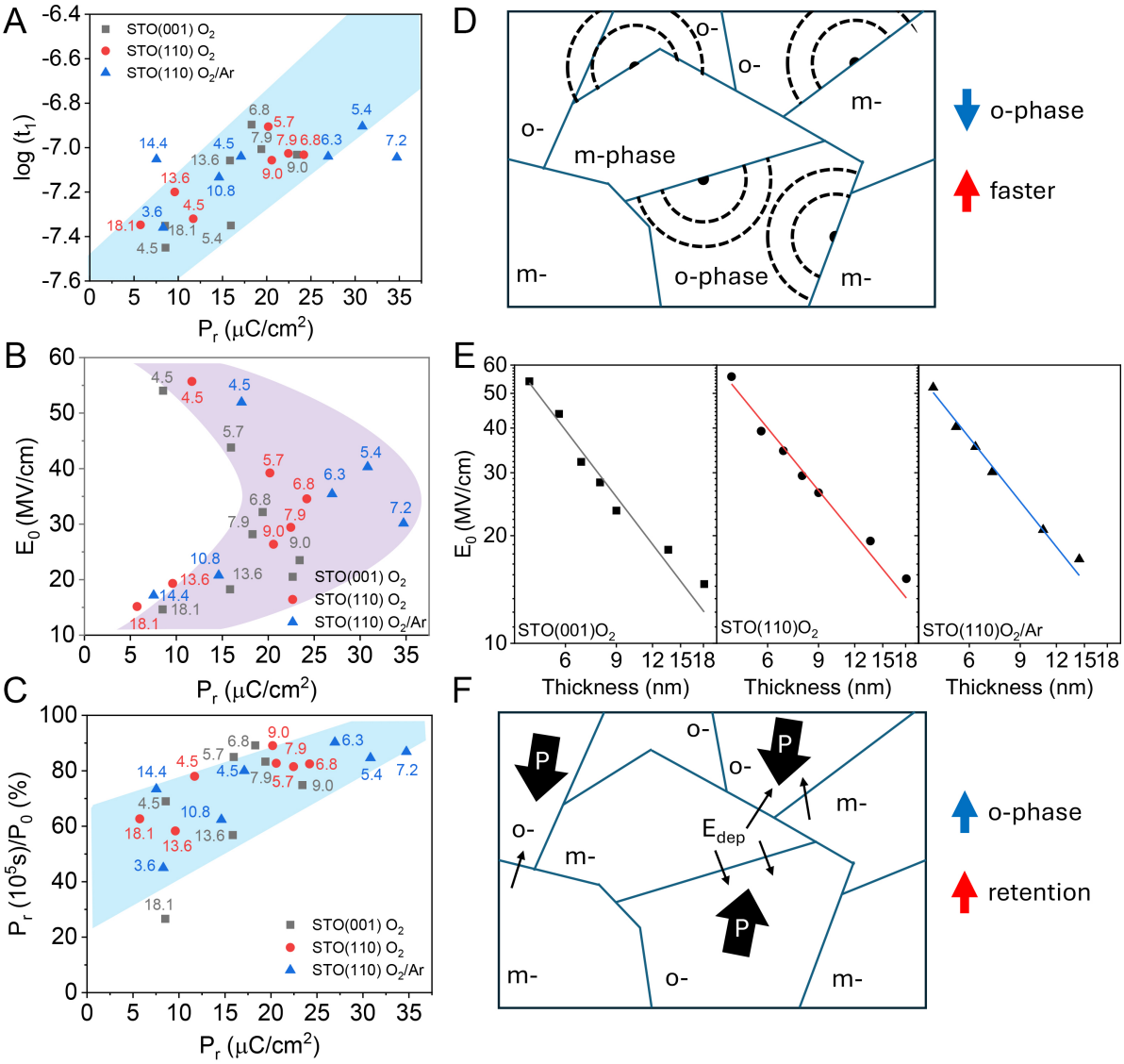

Figure 7. Correlation between switching dynamics and reliability metrics as a function of remanent polarization. (A) Positive switching time as a function of P_r. (B) Characteristic E_0 as a function of P_r. (C) Retention expressed as P_r (10^5 s)/P_0 as a function of P_r. (D) Schematic illustration of the larger number of nucleation sites promoting faster switching in films containing monoclinic/orthorhombic grain boundaries. (E) log-log dependence of E_0 on thickness; the slope is close to 1 in all cases. (F) Sketch of the enhanced in-plane depolarization field E_{dep} in films with a larger presence of monoclinic/orthorhombic phase fraction. Black arrows labeled P denote the polarization direction.

normalized retention $P_r(10^5\ s)/P_0$ smoothly increases as the polarization increases. Note that here retention is evaluated by P_r at 10^5 s, rather than the value extrapolated to 10 years, as done in Figure 6. This approach avoids introducing additional uncertainty associated with long-term extrapolation and provides a direct comparison of the experimentally measured retention across samples. This behavior indicates that larger polarization stabilizes the ferroelectric state and suppresses depolarization-driven back-switching, leading to improved retention. The results obtained in samples grown under O_2/Ar atmosphere do not show systematically decreased retention. This behavior suggests that higher oxygen vacancy concentrations under reducing conditions tailor the stabilization of the orthorhombic phase, increasing polarization [Figure 2C], but do not introduce additional depolarization mechanisms that reduce retention. The corresponding dependences for negative switching time and retention for negative polarity are shown in Supplementary Figure 12.

To summarize, it is observed that as the film thickness increases, the fraction of the monoclinic phase gradually increases, while the remanent polarization initially increases and then decreases as the orthorhombic ferroelectric phase becomes less stable in thicker films. The switching becomes faster in films containing a larger content of the monoclinic phase, indicating that grain boundaries between monoclinic and orthorhombic grains may act as nucleation centers, thus increasing the switching speed [Figure 7D][40]. The dielectric breakdown field decreases monotonically with thickness. Figure 7E shows the dependence of E_{BD} on thickness in a log-log plot, including data fitting following the relation $E_{BD} \propto t^{-n}$ for the three series[41]. In all cases, the extracted exponent value is close to $n \approx 1$. An exponent near 1 suggests dielectric failure governed by interface-limited carrier injection and/or interfacial redox processes, rather than by bulk effects or the density of orthorhombic/monoclinic grain boundaries[41]. The retention stability improves with polarization and reaches optimal values in the intermediate thickness regime. The improved retention is consistent with a reduction in the depolarization electric fields (E_{dep})[42-44]. Thus, when the fraction of the orthorhombic phase decreases at the expense of the monoclinic one, in-plane depolarization fields (E_{dep}) are promoted [Figure 7F]. These fields ultimately favor back-switching of the out-of-plane polarization, leading to poorer retention, as suggested in previous studies of La-doped HfO_2 films[45]. These competing trends highlight the existence of an optimal window where large polarization, stable retention, and acceptable breakdown strength can be simultaneously achieved. In the present films, this optimal region occurs at intermediate thicknesses of approximately 5-10 nm.

CONCLUSIONS

In this work, we investigated the influence of substrate orientation, growth atmosphere, and thickness on the switching behavior and reliability of epitaxial HZO films. Structural analysis shows that the ferroelectric orthorhombic phase is preferentially stabilized for thinner films, while increasing thickness promotes the formation of the monoclinic phase. The largest remanent polarization (above 30 $\mu C/cm^2$) is obtained for films in the intermediate thickness range (5-10 nm). Switching spectroscopy reveals polarity-dependent switching kinetics in thinner films, attributed to built-in electric fields. Reliability measurements further show that the breakdown field decreases with thickness, while retention remains stable in the intermediate thickness range. Thus, detrimental properties are found in the thinnest films, due to a larger contribution of interface-related defects, and in the thicker films, where the orthorhombic phase ratio decreases. Switching speed is found to be favored by the presence of the monoclinic phase. The presented results provide guidelines for the design of ferroelectric tunnel junctions and other resistive switching devices, where the coexistence of oxygen vacancies and ferroelectricity can lead to enhanced device performance[31]. Overall, these results demonstrate that phase stabilization and interface asymmetry govern the switching dynamics and reliability of epitaxial HZO films, providing guidelines for optimizing ferroelectric hafnia-based devices.

DECLARATIONS

Acknowledgments

We acknowledge the assistance of the ICMAB-CSIC Scientific & Technical Services: Thin Films Laboratory (Raul Solanas) and X-ray Diffraction Laboratory (Anna Crespi, Joan Esquius, and Francisco Javier Campos). Lyu, X. 's work was done as part of his Ph.D. program in Materials Science at Universitat Autònoma de Barcelona.

Authors' contributions

Contributed to the acquisition of data, interpretation of the results, formal analysis of the data, and participated in the critical revision of the manuscript: Lyu, X.

Contributed to the acquisition of data, interpretation of the results, formal analysis of the data, and drafted the original manuscript: Ali, F.

Contributed to the conceptualization, data analysis, and interpretation; critically revised the manuscript for

important intellectual content; and provided administrative, technical, and material support for the project: Sánchez, F.; Fina, I.

Availability of data and materials

The original contributions presented in this study are included in the article and Supplementary Materials. Further inquiries can be directed to the corresponding author.

AI and AI-assisted tools statement

During preparation of the initial manuscript draft in March-April 2026, the authors used GPT-5.4 mini (OpenAI; released 2026-03-17) and Gemini 3.1 Pro (Google; released 2026-02-19) to assist with text drafting and language editing. The authors reviewed and revised the generated text and verified all scientific statements. The tools were not used to design the study, collect or analyze data, or determine the interpretation and conclusions. All authors take full responsibility for the accuracy, integrity, and final content of the manuscript.

Financial support and sponsorship

Financial support from the Spanish Ministry of Science, Innovation and Universities (MCIN/AEI/10.13039/501100011033), through the Severo Ochoa MATRANS42 (CEX2023-001263-S) and CEX2023-001286-S, and PID2023-147211OB-C21 projects, is acknowledged. This project has received funding from the European Union's Horizon 2020 research and innovation programme under the Marie Skłodowska-Curie grant agreement No. 101152199. Lyu, X. was supported by the China Scholarship Council (CSC) under grant No. 202206180011.

Conflicts of interest

All authors declared that there are no conflicts of interest.

Ethical approval and consent to participate

Not applicable.

Consent for publication

Not applicable.

Supplementary Materials

Supplementary Materials

REFERENCES

1. Böscke, T. S.; Müller, J.; Bräuhaus, D.; Schröder, U.; Böttger, U. Ferroelectricity in hafnium oxide thin films. *Appl. Phys. Lett.* **2011**, *99*, 102903. DOI
2. Shao, M.; Zhao, R.; Liu, H.; et al. Challenges and recent advances in HfO_2-based ferroelectric films for non-volatile memory applications. *Chip* **2024**, *3*, 100101. DOI
3. Yang, W.; Yu, C.; Li, H.; et al. Ferroelectricity of hafnium oxide-based materials: Current status and future prospects from physical mechanisms to device applications. *J. Semicond.* **2023**, *44*, 053101. DOI
4. Schroeder, U.; Park, M. H.; Mikolajick, T.; Hwang, C. S. The fundamentals and applications of ferroelectric HfO_2. *Nat. Rev. Mater.* **2022**, *7*, 653-69. DOI
5. Materano, M.; Lomenzo, P. D.; Kersch, A.; Park, M. H.; Mikolajick, T.; Schroeder, U. Interplay between oxygen defects and dopants: effect on structure and performance of HfO_2-based ferroelectrics. *Inorg. Chem. Front.* **2021**, *8*, 2650-72. DOI
6. Park, M. H.; Lee, D. H.; Yang, K.; et al. Review of defect chemistry in fluorite-structure ferroelectrics for future electronic devices. *J. Mater. Chem. C.* **2020**, *8*, 10526-50. DOI
7. Lee, J.; Yang, K.; Kwon, J. Y.; et al. Role of oxygen vacancies in ferroelectric or resistive switching hafnium oxide. *Nano. Converg.* **2023**, *10*, 55. DOI PubMed PMC

8. Lee, Y.; Jeong, H. W.; Kim, S. H.; Yang, K.; Park, M. H. Effect of stress on fluorite-structured ferroelectric thin films for semiconductor devices. *Mater. Sci. Semicond. Process.* **2023**, *160*, 107411. DOI
9. Materano, M.; Mittmann, T.; Lomenzo, P. D.; et al. Influence of oxygen content on the structure and reliability of ferroelectric $Hf_xZr_{1-x}O_2$ layers. *ACS. Appl. Electron. Mater.* **2020**, *2*, 3618-26. DOI
10. Kumar, G.; Paul, A.; Das, A.; Larrieu, G.; De, S. Insights into oxygen vacancy effects on ferroelectric behavior of hafnium oxide: a review. *Physica. Status. Solidi.* **2025**, *222*, 2500376. DOI
11. Schroeder, U.; Yurchuk, E.; Müller, J.; et al. Impact of different dopants on the switching properties of ferroelectric hafniumoxide. *Jpn. J. Appl. Phys.* **2014**, *53*, 08LE02. DOI
12. Schroeder, U.; Materano, M.; Mittmann, T.; Lomenzo, P. D.; Mikolajick, T.; Toriumi, A. Recent progress for obtaining the ferroelectric phase in hafnium oxide based films: impact of oxygen and zirconium. *Jpn. J. Appl. Phys.* **2019**, *58*, SL0801. DOI
13. Wei, Y.; Nukala, P.; Salverda, M.; et al. A rhombohedral ferroelectric phase in epitaxially strained $Hf_{0.5}Zr_{0.5}O_2$ thin films. *Nat. Mater.* **2018**, *17*, 1095-100. DOI
14. Lyu, J.; Fina, I.; Solanas, R.; Fontcuberta, J.; Sánchez, F. Robust ferroelectricity in epitaxial $Hf_{1/2}Zr_{1/2}O_2$ thin films. *Appl. Phys. Lett.* **2018**, *113*, 082902. DOI
15. Estandía, S.; Dix, N.; Chisholm, M. F.; Fina, I.; Sánchez, F. Domain-matching epitaxy of ferroelectric $Hf_{0.5}Zr_{0.5}O_2(111)$ on $La_{2/3}Sr_{1/3}MnO_3(001)$. *Cryst. Growth. Des.* **2020**, *20*, 3801-6. DOI
16. Schimpf, J.; Zhang, W.; Manna, M.; et al. Interface effects in the phase determination of $Hf_{0.5}Zr_{0.5}O_2$ epitaxial thin films. *APL. Mater.* **2025**, *13*, 011104. DOI
17. Huang, C.; Zhang, Y.; Zheng, S.; Yang, Q.; Liao, M. Interface effects induced by aZrO_2 seed layer on the phase stability and orientation of HfO_2 ferroelectric thin films: a first-principles study. *Phys. Rev. Appl.* **2021**, *16*, 044048. DOI
18. Shi, S.; Xi, H.; Cao, T.; et al. Interface-engineered ferroelectricity of epitaxial $Hf_{0.5}Zr_{0.5}O_2$ thin films. *Nat. Commun.* **2023**, *14*, 1780. DOI PubMed PMC
19. Jiao, P.; Li, J.; Xi, Z.; et al. Ferroelectric $Hf_{0.5}Zr_{0.5}O_2$ thin films deposited epitaxially on (110)-oriented $SrTiO_3$. *Appl. Phys. Lett.* **2021**, *119*, 252901. DOI
20. Lyu, X.; Ali, F.; Song, T.; Fina, I.; Sánchez, F. Cooperative effects of interface symmetry, redox conditions and low-thickness to improve polarization in ferroelectric $Hf_{0.5}Zr_{0.5}O_2$ films. *ACS. Appl. Mater. Interfaces.* **2025**, *17*, 32596-603. DOI PubMed PMC
21. Song, T.; Tan, H.; Estandía, S.; et al. Improved polarization and endurance in ferroelectric $Hf_{0.5}Zr_{0.5}O_2$ films on $SrTiO_3(110)$. *Nanoscale* **2022**, *14*, 2337-43. DOI
22. Yun, Y.; Buragohain, P.; Li, M.; et al. Intrinsic ferroelectricity in Y-doped HfO_2 thin films. *Nat. Mater.* **2022**, *21*, 903-9. DOI
23. Song, T.; Solanas, R.; Qian, M.; Fina, I.; Sánchez, F. Large enhancement of ferroelectric polarization in $Hf_{0.5}Zr_{0.5}O_2$ films by low plasma energy pulsed laser deposition. *J. Mater. Chem. C.* **2022**, *10*, 1084-9. DOI
24. Mittmann, T.; Materano, M.; Lomenzo, P. D.; et al. Origin of ferroelectric phase in undoped HfO_2 films deposited by sputtering. *Adv. Mater. Inter.* **2019**, *6*, 1900042. DOI
25. Mittmann, T.; Michailow, M.; Lomenzo, P. D.; et al. Stabilizing the ferroelectric phase in HfO_2-based films sputtered from ceramic targets under ambient oxygen. *Nanoscale* **2021**, *13*, 912-21. DOI
26. Lyu, X.; Song, T.; Quintana, A.; Fina, I.; Sánchez, F. Highly stable epitaxially crystallized ferroelectric $Hf_{0.5}Zr_{0.5}O_2$ films. *ACS. Appl. Electron. Mater.* **2023**, *5*, 6142-8. DOI
27. Buragohain, P.; Erickson, A.; Mimura, T.; Shimizu, T.; Funakubo, H.; Gruverman, A. Effect of film microstructure on domain nucleation and intrinsic switching in ferroelectric Y:HfO_2 thin film capacitors. *Adv. Funct. Mater.* **2021**, *32*, 2108876. DOI
28. Li, Y.; Xu, Z.; Li, X.; et al. Unveiling the role of domain wall propagation in enhancing switching properties of ferroelectric Ga-doped HfO_2 thin films. *Mater. Today. Chem.* **2025**, *49*, 103091. DOI
29. Ali, F.; Song, T.; Sánchez, F.; Fina, I. Fast switching and high polarization in ferroelectric $Hf_{0.5}Zr_{0.5}O_2$ films. *Small. Sci.* **2026**, *6*, e202500465. DOI PubMed PMC
30. Lee, D. H.; Lee, Y.; Yang, K.; et al. Domains and domain dynamics in fluorite-structured ferroelectrics. *Appl. Phys. Rev.* **2021**, *8*, 021312. DOI
31. Kim, J.; Shin, W.; Koo, R.; et al. Hybrid ferroelectric-ionic memristive hardware for high scalability in-memory computing. *Nat. Commun.* **2026**, *17*, 6687. DOI PubMed PMC
32. Fina, I.; Fàbrega, L.; Langenberg, E.; et al. Nonferroelectric contributions to the hysteresis cycles in manganite thin films: A comparative study of measurement techniques. *J. Appl. Phys.* **2011**, *109*, 074105. DOI

33. Song, T.; Koutsogiannis, P.; Magén, C.; Pardo, J. A.; Sánchez, F.; Fina, I. Improved polarization-retention-endurance in $Hf_{0.5}Zr_{0.5}O_2$ films by ZrO_2 capping via electrostatic effects. *Adv. Elect. Mater.* **2023**, *10*, 2300509. DOI
34. Zhang, Q.; Li, X.; Zhu, J. Direct observation of interface-dependent multidomain state in the $BaTiO_3$ tunnel barrier of a multiferroic tunnel junction memristor. *ACS. Appl. Mater. Interfaces.* **2021**, *13*, 43641-7. DOI
35. Estandía, S.; Cao, T.; Mishra, R.; Fina, I.; Sánchez, F.; Gazquez, J. Insights into the atomic structure of the interface of ferroelectric $Hf_{0.5}Zr_{0.5}O_2$ grown epitaxially on $La_{2/3}Sr_{1/3}MnO_3$. *Phys. Rev. Mater.* **2021**, *5*, 074410. DOI
36. Chatterjee, S.; Kumar, S.; Gaidhane, A.; Dabhi, C. K.; Chauhan, Y. S.; Amrouch, H. Ferroelectric FDSOI FET modeling for memory and logic applications. *Solid. State. Electron.* **2023**, *200*, 108554. DOI
37. Tagantsev, A. K.; Stolichnov, I.; Setter, N.; Cross, J. S.; Tsukada, M. Non-Kolmogorov-Avrami switching kinetics in ferroelectric thin films. *Phys. Rev. B.* **2002**, *66*, 214109. DOI
38. Weibull, W. A statistical distribution function of wide applicability. *J. Appl. Mech.* **1951**, *18*, 293-7. DOI
39. Huang, T.; Li, Y.; Chen, C.; et al. Demonstration of robust breakdown reliability and enhanced endurance in gallium doped HfO_2 ferroelectric thin films. *IEEE. Electron. Device. Lett.* **2023**, *44*, 1476-9. DOI
40. Song, T.; Sánchez, F.; Fina, I. Impact of non-ferroelectric phases on switching dynamics in epitaxial ferroelectric $Hf_{0.5}Zr_{0.5}O_2$ films. *APL. Mater.* **2022**, *10*, 031108. DOI
41. Stathis, J. H. Percolation models for gate oxide breakdown. *J. Appl. Phys.* **1999**, *86*, 5757-66. DOI
42. Wurfel, P.; Batra, I. P. Depolarization-field-induced instability in thin ferroelectric films-experiment and theory. *Phys. Rev. B.* **1973**, *8*, 5126-33. DOI
43. Mehta, R. R.; Silverman, B. D.; Jacobs, J. T. Depolarization fields in thin ferroelectric films. *J. Appl. Phys.* **1973**, *44*, 3379-85. DOI
44. Kim, D. J.; Jo, J. Y.; Kim, Y. S.; et al. Polarization relaxation induced by a depolarization field in ultrathin ferroelectric $BaTiO_3$ capacitors. *Phys. Rev. Lett.* **2005**, *95*, 237602. DOI
45. Mehmood, F.; Hoffmann, M.; Lomenzo, P. D.; et al. Bulk depolarization fields as a major contributor to the ferroelectric reliability performance in lanthanum doped $Hf_{0.5}Zr_{0.5}O_2$ capacitors. *Adv. Mater. Inter.* **2019**, *6*, 1901180. DOI